Special Issue Contributions

Erin Farrell and Sadhan C. Jana*

Surfactant-free oil-in-oil emulsion-templating of polyimide aerogel foams

https://doi.org/10.1515/ipp-2022-4248
Received June 10, 2022; accepted June 27, 2022;
published online July 14, 2022

Abstract: A surfactant-free oil-in-oil emulsion-templating method is presented for fabrication of monolithic polyimide aerogel foams using monomer systems that produce fast sol–gel transition. An aerogel foam is a high porosity (~90%) material with coexisting meso- and macropores inherent to aerogels with externally introduced micrometer size open cells (macrovoids) that are reminiscent of foams. The macrovoids are introduced in polyimide sol using surfactant-free emulsion-templating of droplets of an immiscible liquid that are stabilized against coalescence by fast sol–gel transition. Three immiscible liquids – cyclohexane, *n*-heptane, and silicone oil – are considered in this work for surfactant-free emulsion-templating. The aerogel foam monoliths, recovered by supercritical drying, exhibit smaller size macrovoids when *n*-heptane and cyclohexane are used as emulsion-templating liquid, while the overall porosity and the bulk density show weak dependence on the emulsion-templating liquid.

Keywords: aerogel foams; aerogels; emulsion-templating; mesoporous materials; polyimide; porous materials.

1 Introduction

Aerogel materials first reported by Kistler (1932) feature high porosity (80–95%) (Kocon et al. 1998) and interconnected pore structures, low density (typically <0.1 g/cm^3) (Duan et al. 2012; Yoldas et al. 2000), and high surface area (200–1000 m^2/g) (Duan et al. 2012, 2013; Zhou et al. 2007). Often, a sol–gel process is used for fabrication of aerogel monoliths (Brinker and Scherer 1990). A wide range of industrial applications benefit from aerogels, such as space exploration (Braun and Manning 2007; Jones 2006), thermal insulation (Baetens et al. 2011), catalysts (Pajonk 1991), and energy storage (Akimov 2003).

Mechanically strong polyimide aerogels were synthesized from a combination of diamines, dianhydrides, and a crosslinker as reported by Kawagishi et al. (2007). Various other polymeric aerogels were reported to date, such as syndiotactic polystyrene (sPS) (Daniel et al. 2008; Wang and Jana 2013), silica (Randall et al. 2011), polyurea (Lee et al. 2009; Leventis et al. 2010; Shinko et al. 2015), and polybenzoxazine (Gu et al. 2015; Mahadik-Khanolkar et al. 2014), but polyimides have been the subject of more extensive investigations due to their importance in NASA's space mission attributed to a set of unique properties, such as thermal and chemical stability (Bessonov et al. 1987). Polyimide aerogels withstand a continuous usage temperature of 250°C and exhibit chemical stability in acids and alkali environments (Androva et al. 1970; Bessonov et al. 1987). Researchers at NASA elaborated the development of various crosslinkers (Guo et al. 2011; Meador 2014; Meador et al. 2015), reinforcement strategies in composite aerogels (Meador et al. 2010), enhanced dielectric properties (Meador et al. 2014), moisture resistance (Meador et al. 2016), and reinforcement of polyimide backbones to achieve higher mechanical properties (Cashman et al. 2020; Guo et al. 2020; Pantoja 2019). These researchers reported polyimide aerogels with a surface area in the range of 200–600 m^2/g, porosity in the range of 78–92%, and bulk density ~0.13 g/cm^3 (Meador et al. 2012).

Polyimide (PI) aerogels offer large fractions of mesopores (pore diameter 2–50 nm) as classified by IUPAC (Mccusker et al. 2001). The mesopores are comparable in size to mean free path of gas molecules. Accordingly, the convective motion of gas molecules within the pores is subdued. This property qualifies polyimide aerogels as thermal insulation materials of cryogenic tanks (Fesmire and Sass 2008), acoustic absorbers (Forest et al. 2001), and thermal insulators for space shuttle antennas (Randall et al. 2011).

Aerogel materials have been produced as films and sheets (Meador et al. 2012), regular shaped monoliths (Duan et al. 2012, 2013), as micrometer size particles (Gu et al. 2016; Lin and Jana 2021; Teo and Jana 2019; Teo

***Corresponding author: Sadhan C. Jana**, School of Polymer Science and Polymer Engineering, University of Akron, Akron, OH 44325-0301, USA, E-mail: janas@uakron.edu
Erin Farrell, School of Polymer Science and Polymer Engineering, University of Akron, Akron, OH 44325-0301, USA

et al. 2020), and as 3D-printed articles of complicated shapes (Teo et al. 2019) with a balance of thermal insulation and load bearing capabilities (Joo et al. 2021). Specifically, aerogel microparticles have strong potential in drug delivery applications (Lin and Jana 2021), thermal insulation (Kistler 1935), and as separation media in packed bed filters to rid airborne particles (Zebida 2011). The unique combinations and interconnectedness of meso- and macropores in polyimide aerogels were exploited in recent research on high efficiency airborne nanoparticle filtration and it was learned that polyimide aerogel pore sizes are dependent on synthesis method and material selection (Zhai and Jana 2017). Mosanenzadeh et al. (2020) reported the role of bimodal pore structures in polyimide aerogels on air permeability. Kim et al. (2015, 2016, 2017) investigated the relationship of aerogel pore fractions and pore sizes with air permeability and filtration efficiency.

This work draws from research on polymers synthesized within the high internal phase emulsions (PolyHIPEs) based on emulsion-templating of polymers that feature high internal phase emulsions (HIPEs) (Menner et al. 2006) with the internal phase accounting for 74% or higher by volume (Menner and Bismarck 2006). Prior work investigated the use of surfactants and salts for stabilization of emulsion before polymerization of the monomers (Pandit et al. 2000; Wong et al. 2013). PolyHIPEs are typically open cell, with interconnected pore networks conducive to permeability of gas and liquids. However, the polymer skin layers in polyHIPEs are impervious and may impede large mass flow (Bhumgara 1995). The stability of emulsions is a concern for HIPEs, although properly selected surfactants render acceptable level of stability (Zapryanov et al. 1983). The research work by Barbetta and Cameron (2004), Silverstein (2014), and Tebboth et al. (2014) discuss several scenarios of emulsion stability.

The work presented in this paper differs from the research on polymer aerogel foams reported by Teo et al. (2018) and Mawhinney and Jana (2019) on the following accounts. First, the aerogel foams produced in earlier work used surfactants for stabilization of emulsified droplets. However, the removal of surfactants from the corresponding gels is a lengthy process. The remnant surfactants often promote moisture absorption due to polar nature and may undergo thermal degradation at low temperature. Second, Teo et al. (2018) and Teo and Jana (2018) considered slow reacting monomer systems for polyimide formulations that needed typically 5–15 min at room temperature for sol–gel transition. Accordingly, surfactants were needed for stabilization of emulsified droplets over a period of 5–15 min. It was also learned from the work of Teo et al. (2018) that not all surfactants are compatible with reactive monomer systems. Mawhinney and Jana (2019) reported the use of high fractions of surfactants ranging from 20-35 wt/vol% to counter the slow gelation process in a polyurea system. Thus, a surfactant-free process should consider fast reacting monomer systems such that fast-forming gels can stabilize the emulsified droplets.

To attain the above objective, we took advantage of the fast reactivity offered by the polyimide monomers, such as pyromellitic dianhydride (PMDA) and *p*-phenylene diamine (PPDA). An additional goal was to study the effects of dispersed volume fractions in the range of 20–40 vol%, instead of 35 vol% considered by Teo et al. (2018). It is noted that a higher volume fraction of macrovoids in the structure of the aerogel can enhance the liquid and gas flow rates through the aerogel foam networks.

The system in the current study was designed to be surfactant-free for a few reasons. It is true that surfactants reduce the interfacial tension in immiscible liquid systems and thus allow emulsion-templating of polyimide gel structures producing narrow macrovoid size distribution. However, a few negative consequences are encountered as well. First, surfactants promote retention of the dispersed liquid within the gel network, e.g., by hydrogen bonding, with unwelcome consequences, such as shrinkage in supercritical drying as was observed in the work of Mawhinney and Jana (2019). Second, the surfactants also produce denser gel networks around the dispersed phase droplets than in the bulk as reported by Teo and Jana (2017) in sPS and Teo et al. (2018) in polyimide aerogel foams.

Figure 1 presents a schematic of how polyimide strands organize in aerogel monoliths creating macro- and mesopores (Figure 1A) and in aerogel foams (Figure 1B) around

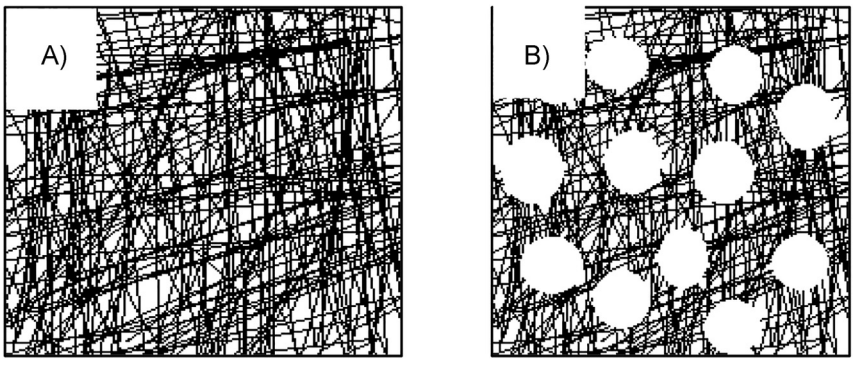

Figure 1: Strands of polyimide (A) and (B) strands of polyimide around macrovoids introduced via emulsion-templating.

the macrovoids created by emulsion-templating. The additional pore structures created by emulsion-templating may expand the potential of these materials for absorption and filtration purposes (Kim et al. 2015, 2016, 2017; Zebida 2011; Zhai and Jana 2017).

An additional attribute of this work is the possibility of accommodating different dispersed liquid phases without recourse to its interactions with the surfactants. This work considered three dispersed oil phases – cyclohexane, *n*-heptane, and silicone oil. It was assumed that the volatile nature of the dispersed phases in this system would be a non-factor due to short reaction times that lead to gelation.

2 Experimental section

2.1 Materials

PMDA with 97% purity and molecular weight (MW) 218.12 g/mol was purchased from Alfa-Aesar (Haverhill, MA, USA). The trifunctional tris(2-aminoethyl) amine (TREN) with 96% purity, and MW 146.23 g/mol, PPDA with 98% purity, and MW 108.14 g/mol, acetic anhydride-ACS reagent with >99% purity and MW 102.09 g/mol, and cyclohexane, ACS reagent were acquired from Sigma Aldrich (Milwaukee, WI, USA). Pyridine-ACS reagent with >99% purity and MW 79.102 g/mol, high temperature silicone oil, and acetone, certified ACS, were purchased from Fisher Scientific (Ontario, NY, USA). *N*,*N*-dimethylformamide (DMF), 99.8%, anhydrous, and *n*-heptane, 99% purity were purchased from VWR International (Radnor, PA, USA).

2.1.1 Fabrication of polyimide aerogels

An oil-in-oil (O/O) emulsion was used in the synthesis process to introduce micrometer sized droplets in the polyimide gel network structure. The solid content in the gel system was calculated based on the weight concentration of the final polyimide products. The stoichiometric ratio of PMDA and PPDA was set at 61:60 for a chain length (n) of 60. This ratio was chosen to obtain a desired chain length between the crosslinks for fair comparison with previous work reported in the literature, such as Teo and Jana (2018) and Teo et al. (2018, 2019). A constant chain length also yielded similar gel times and crosslink density. The 61:60 stoichiometric ratio produced chains with dianhydride ends for crosslinking with a trifunctional amine. Polyimide solutions were prepared by first dissolving the diamine PPDA and dianhydride PMDA separately in DMF and then stirring together for 2 min at 1200 revolutions per minute (RPM) to yield a polyamic acid. TREN, acetic anhydride, and pyridine were added simultaneously and stirred for 30 s to yield the polyimide sol. The structures of diamine, dianhydride, crosslinked polyamic acid, and crosslinked polyimide are shown in Figure 2. The dispersed phase (cyclohexane, silicone oil, or *n*-heptane) was introduced to the sol and stirred for an additional 30 s. A typical polyimide sample at 10 wt% polymer concentration with 30 vol% dispersed phase is prepared with a total volume of 7.5 ml and 0.3724 g PMDA, 0.1816 g PPDA, 0.0056 g TREN, 1.2912 ml acetic anhydride, 1.1048 ml pyridine, 4.66 ml DMF, and 2.25 ml of the dispersed liquid.

The reaction was conducted at room temperature (20°C) in a sealed glass vial. The final sol or emulsion-templated sol was poured into cylindrical molds and allowed to gel for 24 h. The wet gels were demolded to facilitate exchange of the solvent from the network structure with acetone. The first two solvent exchanges were carried out using mixed solvents of volume ratio of DMF and acetone at 75/25 and 25/75. The wet gels were then exchanged with 100% acetone three times, allowing 24 h for each exchange. The acetone filled gels were placed in the supercritical drying chamber to conduct solvent exchanges with liquid CO_2. Supercritical drying was conducted at 50°C and 11 MPa to obtain aerogels.

In this work, the polyimide gels were prepared with 20, 30, and 40 vol% of the dispersed liquid named. The specimens are designated in the rest of the manuscript as 80–20, 70–30, and 60–40. The control sample refers to a polyimide aerogel produced without emulsion-templating.

2.2 Characterization

2.2.1 Interfacial tension measurement

The interfacial tension between the continuous phase DMF and the dispersed phases, e.g., cyclohexane, *n*-heptane, or silicone oil was measured via a Du Noy tensiometer (Interfacial Tensiometer 70545, CSC Scientific Co., Fairfax, VA, USA). DMF was poured into a glass container followed by addition of 20 ml of dispersed phase by pouring the liquid over a glass slide at an angle to form a clean interface. The interfacial tension value was recorded in triplicate with the use of the Du Noy ring at room temperature (20°C).

2.2.2 Emulsion droplet size

The size of dispersed phase oil droplets was first registered by placing 100 µl of the emulsion on a microscope slide with a depression and taking the images of droplets using an optical microscope (model BX51, Olympus, Center Valley, PA, USA). The images were analyzed using ImageJ

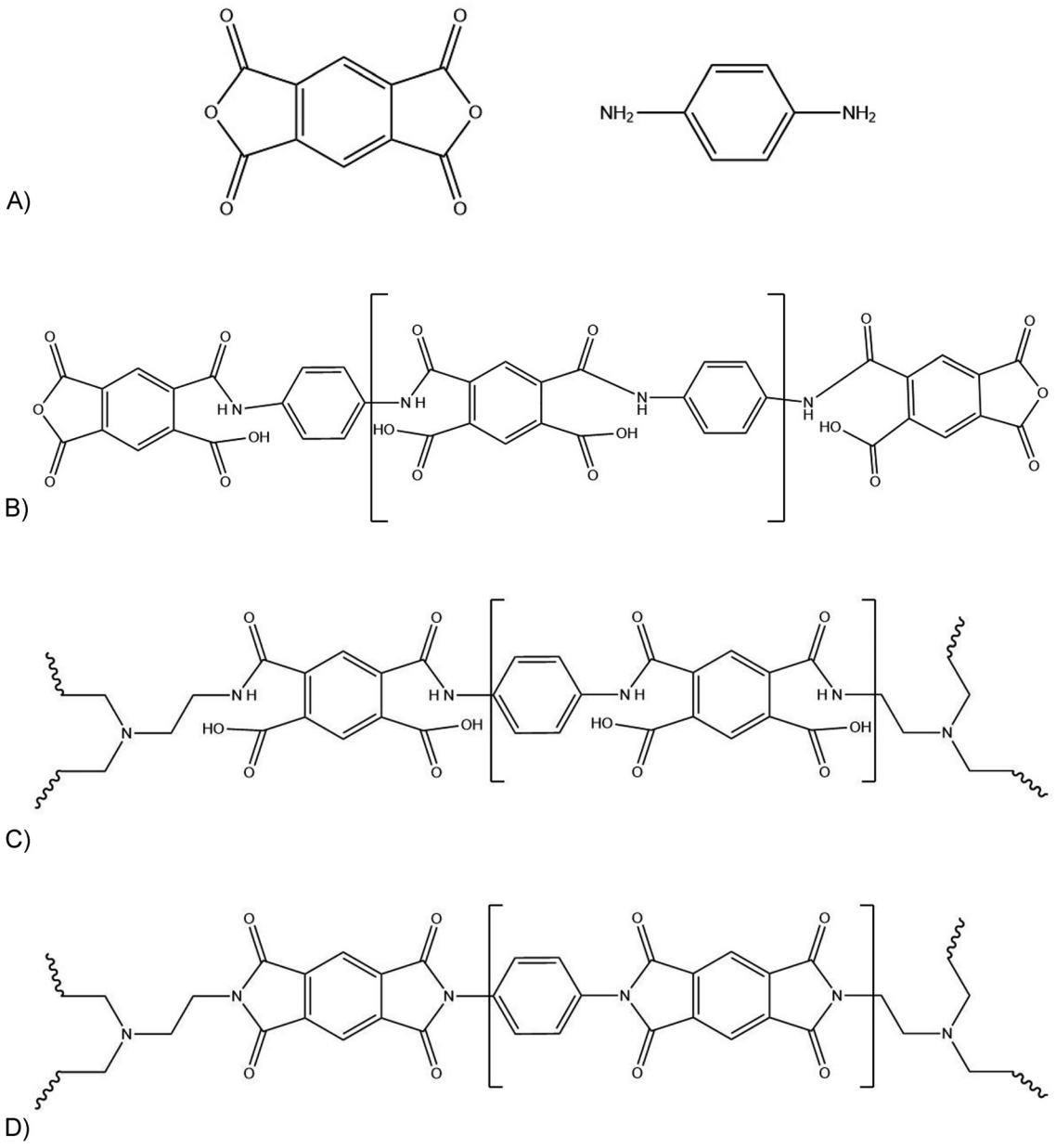

Figure 2: Molecular structures of (A) pyromellitic dianhydride and *p*-phenylene diamine monomers, (B) polyamic acid, (C) crosslinked polyamic acid, and (D) crosslinked polyimide.

software (National Institute of Health, Bethesda, MD, USA) to obtain a population of droplet diameter and the corresponding distribution with the diameter of at least 200 individual drops analyzed.

2.2.3 Gel time

The gel time for the polyimide sol was estimated at room temperature (20°C) via tilting method. At the gel time, the liquid meniscus in the mold did not move when the mold was tilted at an angle of 25°.

2.2.4 Porosity and pore volume

Porosity was calculated from the values of bulk (ρ_b) and skeletal (ρ_s) density using equation (1):

$$\text{Porosity}\,(\pi) = \left(1 - \frac{\rho_b}{\rho_s}\right) \times 100\,\%\,. \tag{1}$$

Bulk density was determined from mass and volume of the aerogel specimens. Skeletal density was determined using helium pycnometer (AccuPyc II 1340, Micromeritics Instrument Corp., Norcross, GA, USA). Total pore volume

(V_{total}) was determined from the values of bulk and skeletal density using equation (2). The volume of macropores (V_{ma}, diameter >50 nm), as shown in equation (3) was obtained from equation (2) and the pore size distribution data from the Tristar II 3020 analyzer (Micromeritics Instrument Corp., Norcross, GA, USA) that provided the values for micropore volume (V_{mi}, diameter> 2 nm) and mesopore volume (V_{ms}, diameter 2–50 nm). The fractions of mesopores (ϕ_{ms}) and macropores (ϕ_{ma}) in aerogels were determined by multiplying overall porosity by the volume fraction of each component, as demonstrated in equation (4):

$$V_{\text{total}} = \frac{1}{\rho_b} - \frac{1}{\rho_s}, \tag{2}$$

$$V_{ma} = V_t - V_{mi} - V_{ms}, \tag{3}$$

$$\phi_{ma} = \frac{\pi V_{ma}}{V_T}; \phi_{ms} = \frac{\pi V_{ms}}{V_T}. \tag{4}$$

2.2.5 Shrinkage

The diameter shrinkage in aerogel foams was determined from the comparison of the diameter of the mold (d_0) and that of the supercritically dried aerogel foam (d), as in equation (5):

$$\text{Shrinkage} = 100\left(1 - \frac{d}{d_0}\right)\%. \tag{5}$$

The diameter of the mold was 1.22 cm.

2.2.6 BET surface area

The Brunauer–Emmett–Teller (BET) surface area of the aerogel was collected via nitrogen adsorption–desorption isotherms at 77K with the Tristar II 3020 (Micromeritics Instrument Corp., Norcross, GA, USA).

2.2.7 Aerogel morphology

Scanning electron microscope (SEM, JSM5310, JEOL, Peabody, MA, USA) was used to study the morphology of the aerogel samples. An accelerating voltage of 5 kV and an emission current of 20 mA were used for sample imaging. A piece of aerogel specimen was mounted on an aluminum stub with carbon tape and sputter coated with silver (ISI-5400 Sputter Coater, Polaron/Quorum, Laughton, UK).

2.2.8 Viscosity

The viscosity values of polyimide sols were obtained from an ARES G2 Rheometer (TA Instruments, New Castle, DE, USA). The rheometer setup had a 50 mm diameter cone and plate arrangement with oscillatory strains at a constant angular frequency of 1 rad/s at 10% strain, as previously established by Teo et al. (2019). The rheological measurements were carried out at room temperature (20°C). The values of complex viscosity versus time were also obtained.

3 Results and discussion

Table 1 lists several properties of the solvents used.

The O/O emulsions were prepared in the absence of precursor monomers for polyimide and used in evaluation of interfacial tension and the distribution of dispersed phase droplet diameter.

The interfacial tension values between the continuous phase DMF and three dispersed phase liquids are listed in Table 2.

It is inferred from Table 2 that the lowest value of interfacial tension, 3.0 mN/m, was found for the liquid pair DMF and silicone oil, followed by DMF/cyclohexane (3.6 mN/m), and DMF/*n*-heptane (4.0 mN/m). The vapor pressure data in Table 1 indicate that silicone oil has the lowest volatility while cyclohexane has the highest volatility among the dispersed phase liquids.

Table 1: Solvent data (Smallwood 2012).

Solvents	Formula	Density (g/cm^3)	Surface tension at 20°C (mN/m)	Viscosity (cp)	Vapor pressure at 21°C (mmHg)
Cyclohexane	C_6H_{12}	0.778	24.98	0.98	78.8
n-Heptane	C_7H_{16}	0.664	19.3	0.41	40
Silicone oil	$C_6H_{18}OSi_2$	0.936	40	95–105	5
Dimethylformamide	C_3H_7NO	0.945	35	0.82	3.8

Table 2: Interfacial tension values without surfactant.

Continuous phase	Dispersed phase	Interfacial tension (mN/m)
N,*N*-dimethylformamide	Silicone oil	3.0 ± 0.1
	n-Heptane	4.0 ± 0.05
	Cyclohexane	3.6 ± 0.1

The size of droplets in O/O emulsion was inferred from optical microscopy images with the aid of ImageJ software. The emulsions were prepared by stirring the DMF continuous phase and one of the dispersed phase liquids listed in Table 2 at 20 and 40% by volume. The diameter of at least 200 individual droplets were taken into account for each analysis and the diameter data were distributed in three size bins at <60, 60–120, and >120 μm, as shown in Figure 3.

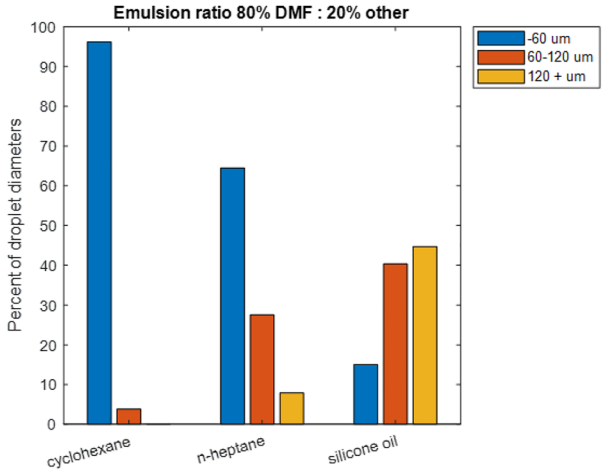

Figure 3: Droplet size distributions, at (A) 20 vol% dispersed phase and (B) 40 vol% dispersed phase.

The breakdown of data into narrower diameter range and greater number of bins did not produce better interpretation. The data revealed that at both 20 and 40% by volume, the emulsions of cyclohexane in DMF exhibited the highest fraction of droplets smaller than 60 μm, while silicone oil produced the highest fraction of droplets with size greater than 120 μm. At 20% by volume, cyclohexane and *n*-heptane emulsions had respectively ~95 and ~65% of droplets smaller than 60 μm. The percent of droplets in the range 60–120 μm increased in all cases for 40 vol% of dispersed liquids. It is noted that the diameter distribution of macrovoids in the final aerogel foams is closely related to diameter distribution of dispersed phase liquid in the precursor emulsion.

Table 3 lists the values of mean, median, maximum, and minimum droplet diameter for each emulsion system inferred from optical microscope images and analyzed using ImageJ software. The results indicate that the smallest mean droplet diameter of 27 ± 12 μm at 20 vol% and 67 ± 30 μm at 40 vol% were obtained in the case of cyclohexane, in line with the lowest interfacial tension value among the three dispersed phase liquids when viscosity was comparable. The emulsions of *n*-heptane and silicone oil exhibited much larger droplets, respectively, 59 ± 35 μm at 20 vol% and 95 ± 44 μm at 40 vol% *n*-heptane and 124 ± 63 μm at 20 vol% and 154 ± 82 μm at 40 vol% silicone oil.

The data in Table 3 also corroborate that an increase of dispersed phase volume percent also increases the mean droplet size, e.g., silicone oil had a mean droplet diameter of 113 and 154 μm, respectively, at 20 and 40 vol %. This is attributed to higher degree of coalescence of droplets at greater volume fraction of the dispersed phase. A more specific break down of diameter and the population of droplets in each diameter range are listed in Table 4.

The data listed in Table 4 indicate that cyclohexane dispersed phase at 20 vol% yielded 96% of measured droplets with diameter less than 60 μm. This group of droplets had a mean diameter of 26 μm. At 40 vol% cyclohexane, the fraction of droplets of diameter less than 60 μm was only 47% with a mean diameter 45 μm, while 47% of the droplets were found in the range of 60–120 μm due to greater degree of coalescence. Similar shifts in droplet population are seen for other dispersed phase liquids. Silicone oil dispersed phase at 20 and 40 vol% had, respectively, 45 and 60% of droplets with diameter greater than 120 μm. We attribute this to higher frequency collision events between dispersed phase droplets. Figure 4 presents a set of representative images used in the generation of droplet size distribution.

Table 3: Mean, median, maximum, and minimum droplet diameter in surfactant-free emulsions in *N*,*N*-dimethylformamide.

Dispersed phase vol%	Dispersed phase	Mean diameter (μm)	Median diameter (μm)	Maximum diameter (μm)	Minimum diameter (μm)
20	Cyclohexane	27 ± 12	25	87	8
	n-Heptane	59 ± 35	45	174	16
	Silicone oil	124 ± 63	113	384	25
40	Cyclohexane	67 ± 30	61	231	23
	n-Heptane	95 ± 44	79	302	42
	Silicone oil	154 ± 82	143	475	30

Table 4: Droplet distribution data and mean diameter in micrometer in each size range.

Dispersed vol%	Dispersed phase	<60 μm diameter		60–120 μm		>120 μm	
		Percent	Mean diameter	Percent	Mean diameter	Percent	Mean diameter
20	Cyclohexane	96	26	4	70	0	
	n-Heptane	65	37	28	87	8	139
	Silicone oil	15	47	40	90	45	179
40	Cyclohexane	47	45	47	79	6	149
	n-Heptane	20	53	56	81	24	162
	Silicone oil	9	52	31	85	60	203

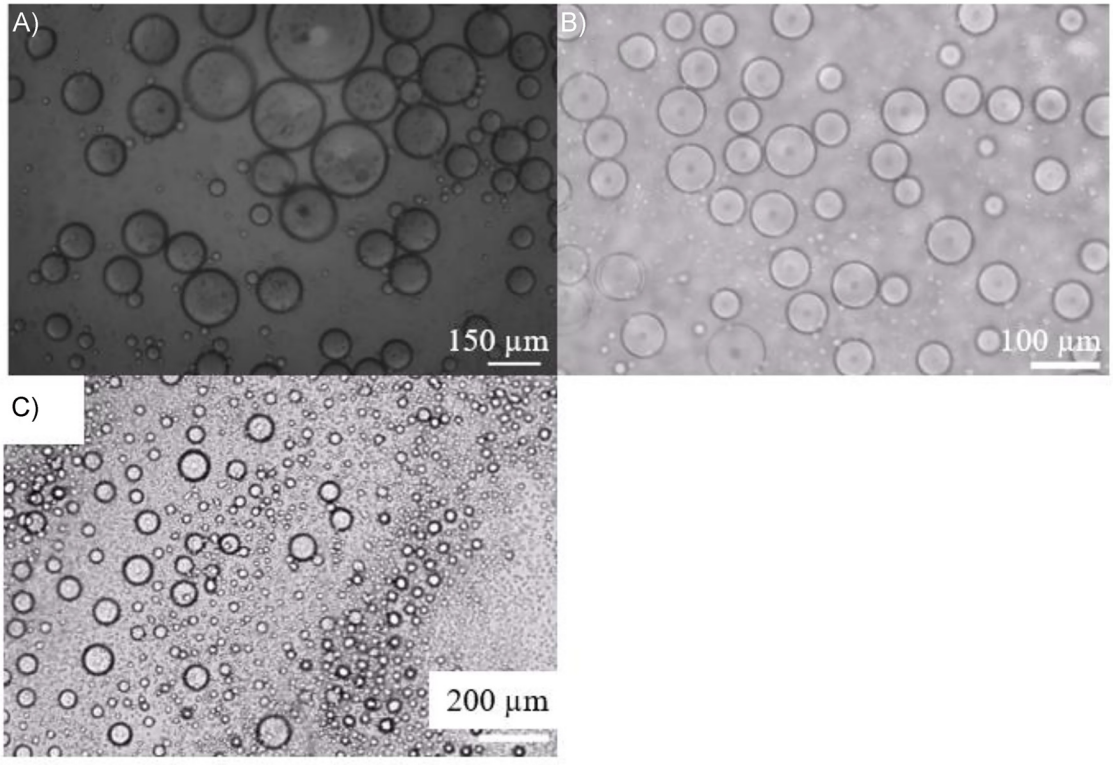

Figure 4: Dispersed phase droplets in *N*,*N*-dimethylformamide at 20°C, A) silicone oil, B) cyclohexane, C) *n*-heptane in 30 vol% of the respective solvent.

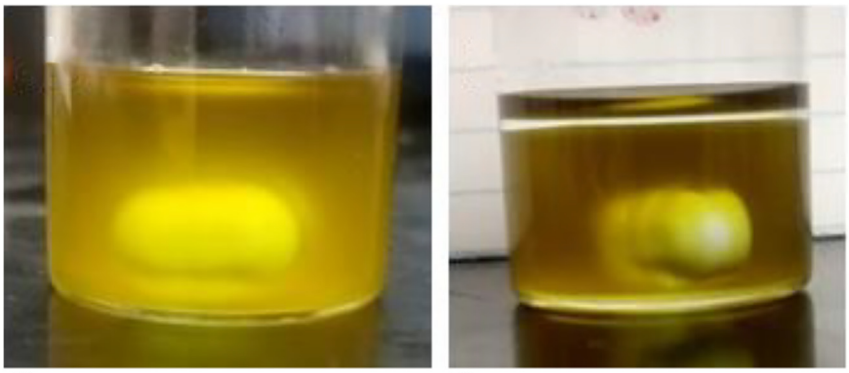

Figure 5: State of emulsion with (A) stirring and (B) creaming after stirring was stopped.

It is known from prior work that O/O emulsions have poor stability due to mutual solubility between the phases (Molau 1965; Smallwood 2012). As per the data presented above and the representative images of droplets in emulsion presented in Figure 4, the largest droplets were found in emulsions of silicone oil, attributed to higher viscosity of silicone oil at 105 cp. The higher viscosity silicone oil needed greater shear force for breakup of the droplets (Nekouei and Vanapalli 2017). The Grace curve for capillary breakup under shear flow also supports the observation of largest droplets in the case of silicone oil (Grace 1982). The ratio (p) of viscosity of silicone oil dispersed phase (η_d) and DMF/polyimide solution continuous phase (η_c) as in equation (6) determines a critical capillary number (Ca_c, equation (7)) in the Grace curve. In equation (7) $\dot{\gamma}$ is shear rate, R is the equilibrium radius of the droplet, and Γ is the interfacial tension.

$$p = \frac{\eta_d}{\eta_c}, \tag{6}$$

$$Ca_c = \frac{\eta_c \dot{\gamma} R_0}{\Gamma}. \tag{7}$$

The shear viscosity of DMF/polyimide solution continuous phase was the same for all formulations, but the value of p varied more significantly for silicone oil dispersed phase yielding larger droplets for silicone oil.

3.1 Emulsion stability

As no surfactant was used in preparation of the emulsion, it was expected at the outset that the emulsions would experience certain degree of instability. In view of this, the time scale of appreciable separation of the dispersed phase liquid was evaluated. As per the density data listed in Table 1, all three dispersed phase liquids – cyclohexane (density 0.778 g/cm^3), n-heptane (density 0.664 g/cm^3), and silicone oil (density 0.936 g/cm^3) – were lighter than polyimide sol prepared in DMF (density 1.0 g/cm^3) and experienced creaming. Figure 5 shows images of the vial containing cyclohexane emulsion just after removal from the stir plate (A) and after separation was complete with a layer of cyclohexane forming at the top of the polyimide sol.

A time-lapse video of separation of the dispersed liquid was recorded and the time for complete separation was noted. For this purpose, the height (h) of the clear liquid layer of the dispersed phase was monitored with time (t) and compared with the initial height (h_0) of the emulsion vial. The creaming rate was inferred from the slope of (h/h_0) versus t curves as shown in Figure 6 and listed in Table 5. As expected, the silicone oil system experienced the slowest creaming (Figure 6B) due to smallest density difference with the polyimide sol. The system with fastest creaming was observed for n-heptane, due to highest density difference with polyimide sol. It is apparent from the data in Table 5 that higher volume fraction of the dispersed phase led to slower creaming. This is counter-intuitive, as greater extent of coalescence and droplets of much larger diameter found at higher dispersed phase volume fractions, as per data in Table 3 and associated discussions, should promote faster creaming.

It is recalled that the data included in Table 5 were obtained using a continuous phase of polyimide sol without the catalyst and the dehydrating agent. Thus, the creaming behavior did not take into consideration the effects of imidization reactions.

The data presented in Figure 6 can be interpreted in terms of terminal velocity of the dispersed droplets. The terminal velocity is the constant speed of a freely rising droplet determined by the balance of form drag and the buoyancy force. An expression of terminal velocity (V_t) is:

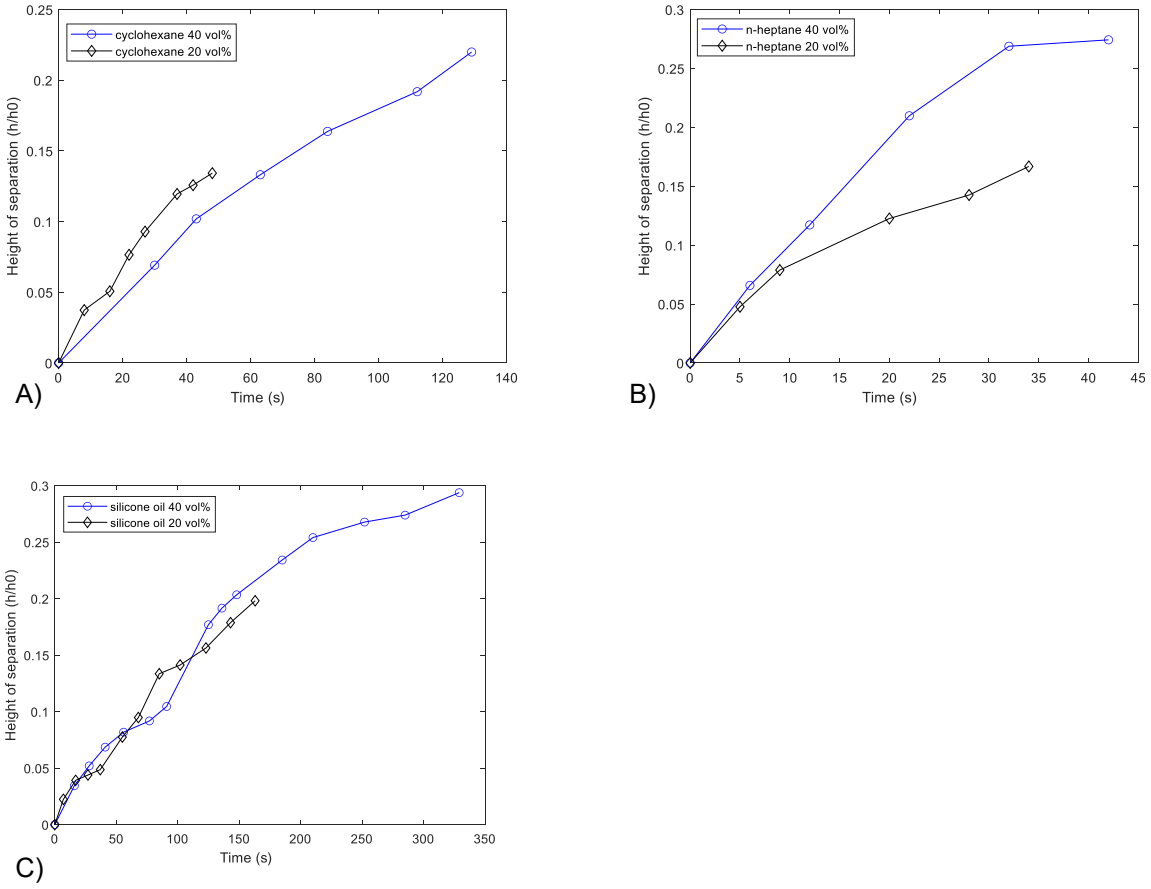

Figure 6: Emulsion separation in polyimide sol versus time for (A) cyclohexane, (B) *n*-heptane, and (C) silicone oil.

Table 5: Emulsion separation times and creaming rates in polyimide sol.

Emulsion	Time to separate (s)	Creaming rate (1/s)
20 vol% cyclohexane	68	0.0028
40 vol% cyclohexane	90	0.0012
20 vol% *n*-heptane	32	0.0045
40 vol% *n*-heptane	45	0.0068
20 vol% silicone oil	210	0.0012
40 vol% silicone oil	330	0.0009

$$V_t = \left(\frac{2}{9}\right)\left(\frac{\rho_p - \rho_f}{\mu}\right) g R^2. \quad (8)$$

In equation (8), $\rho_p$is the density of the dispersed phase droplet, ρ_f is the density of DMF, μ is the viscosity of the polyimide sol, g is gravity, and R is the radius of the dispersed droplet. It is noted that equation (8) does not account for the volume fraction of the dispersed phase and is applicable for the motion of a single droplet.

The viscosity of polyimide sol increased with time due to crosslinking and imidization reactions (see Figure 7). The viscosity did not change much initially, e.g., up to ~60 s, but increased in exponential fashion as the gelation point was approached. Accordingly, the terminal velocity value reduced appreciably with time as per equation (8). The higher terminal velocity and faster creaming are inferred for larger droplets. The counterintuitive results seen from the data in Table 5, e.g., slower creaming at higher volume fractions of dispersed liquids can now be attributed to "crowding" (Abbott 2017) caused by an increase of the viscosity of the emulsion. Richardson and Zaki (1959) reported a relationship between the effective terminal velocity $V_{t,eff}$ with dispersed phase volume fraction (ϕ) and single droplet terminal velocity V_t as in equation (9). The value of $V_{t,eff}$ is lower than V_t at non-zero values of ϕ.

$$V_{t,eff} = V_t \times (1 - \phi)^{4.65}. \quad (9)$$

Equation (9) indicates that the terminal velocity decreases with an increase of dispersed phase liquid volume. This explains the experimental data and the creaming times reported in Table 5. In Figure 8, the terminal velocity calculated based on equation (9) are plotted versus time

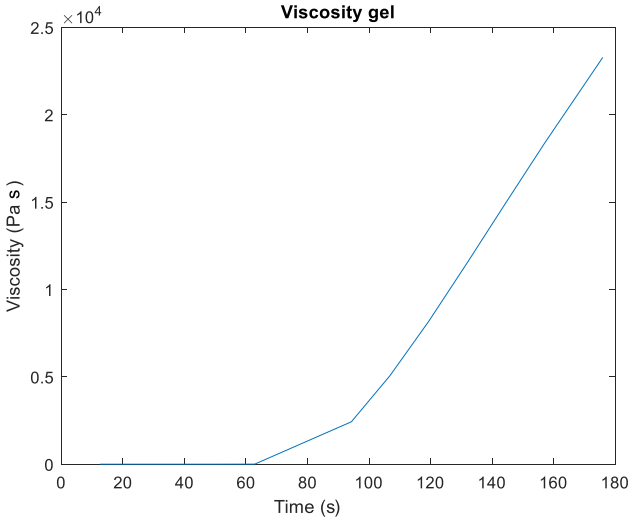

Figure 7: Viscosity of polyimide sol with time.

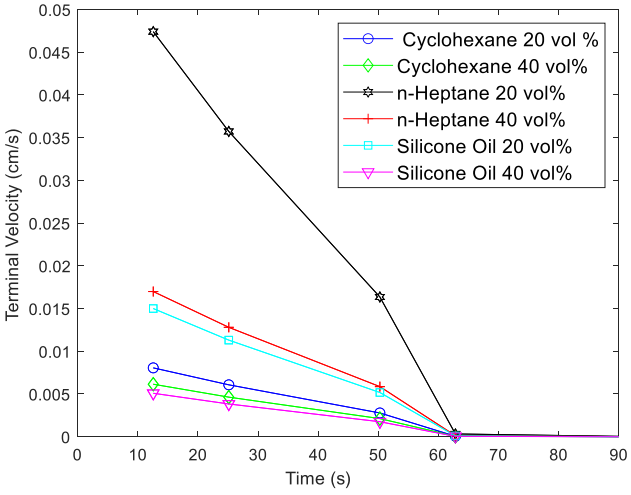

Figure 8: Theoretical terminal velocity of droplets over time.

after considering an increase of the value of viscosity μ, as per data presented in Figure 7. It is apparent that emulsions with 20 vol% dispersed liquid show higher terminal velocity and faster creaming corroborating the experimental data reported in Figure 6 and Table 5.

3.2 Gel times

The data in Figure 9 show dependence of gelation time of polyimide sol on volume fraction of dispersed phase liquids cyclohexane, *n*-heptane, and silicone oil. For a given dispersed phase volume fraction, the longest gelation time is seen for cyclohexane and the shortest for silicone oil. The data also show longer gelation time at higher volume fraction of the dispersed phase. For example, at 20 vol% dispersed phase, the gelation times are 68, 62, and 52 s, respectively, for cyclohexane, *n*-heptane, and silicone oil. The gelation time increased to 88, 80, and 66 s for the same dispersed phases at 35 vol%.

Teo et al. (2018) and Teo and Jana (2018) reported that the surfaces of dispersed phase droplets trigger heterogenous nucleation of polyimide domains much earlier than the bulk. Also, such heterogenous nucleation produces much denser gel networks than in the bulk. Accordingly, the bulk of the liquid sees depletion of polyimide precursor materials which is accentuated at higher volume fraction of the dispersed phase leading to an extended gelation time, as also reported by Mawhinney and Jana (2019). It is seen in Figure 9 that silicone oil-templated samples underwent fastest gelation while cyclohexane took the longest time for gelation for the same dispersed phase volume percent. It

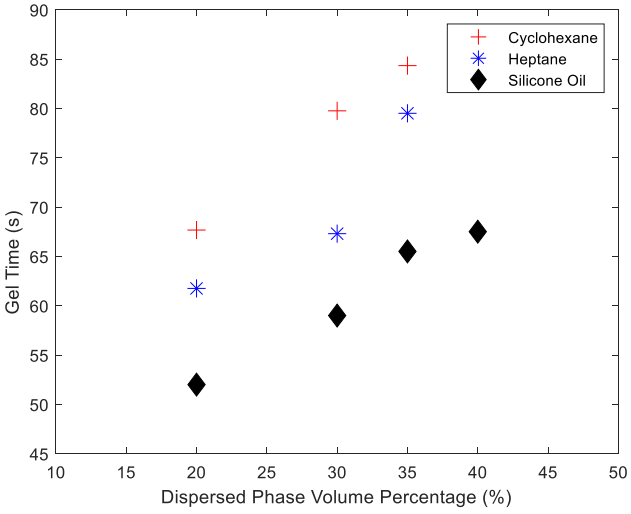

Figure 9: Gel time as a function of dispersed phase volume.

was seen from the data in Table 3 that cyclohexane produced the smallest droplets in emulsion in DMF, thus offering highest surface area to volume ratio for nucleation among the three dispersed phase liquids.

3.3 Aerogel foam materials

Data on porosity, density, shrinkage, BET surface area, and pore volume are collected and correlated to the emulsion composition. Table 6 lists the data for bulk density, porosity, shrinkage, and volume percentages of emulsion-templated aerogel samples.

Table 6: Bulk density, shrinkage, porosity, and percent pores in macro- and mesopore range of emulsion-templated polyimide aerogel foams.

Material	Bulk density (g/cm^3)	Shrinkage (%)	Porosity (%)	Macropore (%)	Mesopore (%)
Control	0.102 ± 0.001	14.0 ± 0.3	88.0 ± 0.2	~55	~33
Cyclohexane					
20 vol%	0.093 ± 0.004	16.0 ± 0.6	94.4 ± 0.4	~88	~6
30 vol%	0.099 ± 0.009	16.2 ± 0.5	94.5 ± 0.5	~89	~6
35 vol%	0.097 ± 0.010	21.0 ± 0.6	94.8 ± 0.3	~89	~6
n-Heptane					
20 vol%	0.094 ± 0.005	16.6 ± 0.5	94.6 ± 0.2	~87	~7
30 vol%	0.096 ± 0.001	17.8 ± 0.7	94.7 ± 0.3	~87	~7
35 vol%	0.096 ± 0.010	23.1 ± 0.3	94.2 ± 0.2	~86	~7
Silicone oil					
20 vol%	0.115 ± 0.001	20.5 ± 0.9	92.8 ± 0.3	~85	~8
30 vol%	0.112 ± 0.006	22.3 ± 0.9	92.0 ± 0.3	~84	~8
35 vol%	0.118 ± 0.004	26.6 ± 0.9	91.4 ± 0.3	~83	~8

3.4 Bulk density

In view of macrovoids accounting for additional pore volumes, the introduction of a dispersed phase liquid in emulsion-templated specimens should reduce the bulk density of aerogel specimens, as shown by Kulkarni and Jana (2021) for aerogel foams of sPs produced via Pickering emulsion method:

$$\phi_T = \phi_{\text{macrovoid}} + \phi_{\text{inherent}}(1 - \phi_{\text{macrovoid}}). \quad (10)$$

In equation (10), ϕ_T, $\phi_{\text{macrovoid}}$, and ϕ_{inherent} are, respectively, the total porosity of the aerogel foam specimen, porosity contributed by the macrovoid, and the inherent porosity of the control aerogel material. Assuming no additional shrinkage due to incorporation of the dispersed phase liquid, equation (10) yields total porosity values of 90.4, 91.6, and 92.2%, respectively, for aerogel foams with 20, 30, and 35 vol% dispersed phase liquids. In these calculations, ϕ_{inherent} was assumed to be the same as the control PI aerogel (88%). It is seen from the data in Table 6 that the total porosity values of aerogel foams in the range of 92–95% were higher than the control specimen but did not change much with an increase of the vol% of the dispersed phase liquid. This may be due to additional shrinkage in aerogel foam specimens encountered in solvent exchange or supercritical drying steps. It was inferred earlier that emulsions took longer times to gel in the presence of higher volume percent of dispersed phase liquid and that heterogenous nucleation at dispersed phase droplet surfaces depleted polyimide concentration in the bulk. This may be the primary reason behind greater shrinkage observed.

The bulk density of aerogel foam specimens obtained using silicone oil as the dispersed phase were higher (0.112–0.118 g/cm^3, Table 6) compared to the control specimen density of 0.102 g/cm^3. This is attributed to higher shrinkage (20–26%) in the former specimens compared to 14% shrinkage in control material. The aerogel foam specimens produced with *n*-heptane and cyclohexane had lower bulk density values (0.094–0.099 g/cm^3), although shrinkage was higher (16–23%).

Table 7: BET surface area.

Dispersed liquid	Cyclohexane (m^2/g)	*n*-Heptane (m^2/g)	Silicone oil (m^2/g)
20 vol%	423 ± 5	445 ± 4	357 ± 4
30 vol%	322 ± 3	399 ± 3	301 ± 2
35 vol%	318 ± 2	320 ± 4	264 ± 2

Control PI aerogel monolith surface area = 620 ± 5 m^2/g.

3.5 BET surface area

The BET surface area values in Table 7 show reduction with increasing amount of dispersed phase for all combinations. The control sample features the highest surface area value at 620 ± 5 m^2/g. The BET surface area values for different dispersed phases follow the same trend as the interfacial tension. Based on the solvent used at 20 vol%, the *n*-heptane dispersed phase reports the highest specific surface area at 445 ± 4 m^2/g, followed by cyclohexane at 423 ± 5 m^2/g, then silicone oil at 357 ± 4 m^2/g. With an increase of dispersed phase liquid content to 35 vol%, the surface areas reduced for cyclohexane, *n*-heptane, and silicone oil with values of 318 ± 2, 320 ± 4, and 264 ± 2 m^2/g, respectively. The introduction of the dispersed phase increases the gelation time and results in the formation of

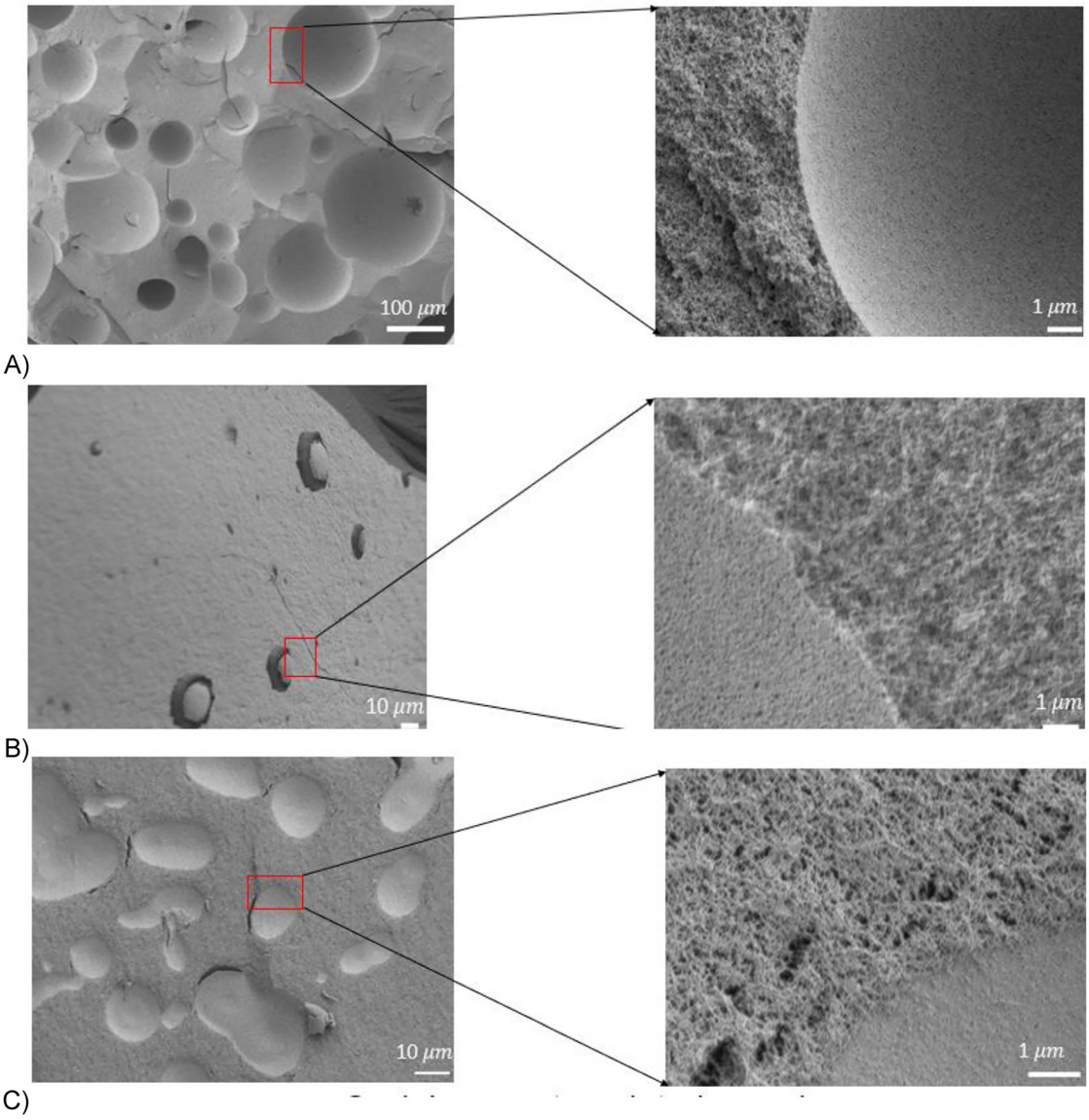

Figure 10: Scanning electron microscope images of aerogel foams produced with (A) silicone oil, (B) *n*-heptane, and (C) cyclohexane.

denser skin layers at the interface. Teo and Jana (2018) discussed polyimide strands and the correlation with gelation time and BET surface area. The BET isotherm data are presented in Figure S1 (see Appendix).

3.6 Macrovoid and pore architecture

The SEM images verify the presence of the macrovoids. A set of representative images are seen in Figure 10. The aerogel foams produced with silicone oil show the most visible macrovoids originating from the large droplets produced in emulsion-templating (see Table 4). Cyclohexane-templated specimens had smaller macrovoids originating from smaller dispersed droplets.

As indicated by the SEM images in Figure 10, the polyimide morphology in and around the macrovoids did not vary much with the use of different emulsion-templating liquids, although the size of the macrovoids varied due to different sizes of emulsified droplets. The examination of representative SEM images at the top, bottom, and middle of specimens indicate that the system did not undergo appreciable creaming prior to polyimide gelation due to an increase of viscosity of the sol, as seen in Figure 7. In view of this, the emulsified droplets were captured within the gel and produced the macrovoids.

4 Conclusions

The findings indicate that the fast-reacting diamine and dianhydride selected in this work led to gelation within 90 s and produced good quality polyimide aerogel foam materials even in the absence of a surfactant. Among the three emulsion-templating liquids, *n*-heptane showed a tendency of fastest creaming while silicone oil showed the slowest creaming, although the continual increase of viscosity of the sol due to fast gelation acted against appreciable creaming in the aerogel foam materials. The porosity of the aerogel foam (92–95%) was higher than the corresponding monolith (88%). All three emulsion-templating liquids produced similar values of porosity and bulk density although the macrovoid sizes were the smallest in the case of cyclohexane and largest in the case of silicone oil. The overall porosity and the co-existing open pores consisting of macrovoids, macropores, and mesopores together will be important for applications such as airborne nanoparticle filtration.

Author contributions: All the authors have accepted responsibility for the entire content of this submitted manuscript and approved submission.

Research funding: This work was funded by Division of Civil, Mechanical and Manufacturing Innovation, National Science Foundation under grant number CMMI 1826030.

Conflict of interest statement: The authors declare no conflicts of interest regarding this article.

References

Abbott, S. (2017). *Surfactant science: principles & practice*. DEStech Publications, Inc., Lancaster.

Akimov, Y.K. (2003). Fields of application of aerogels (review). Instrum. Exp. Tech. 46: 287–299, https://doi.org/10.1023/A:1024401803057.

Androva, N.A., Bessonov, M.I., Laius, L.A., and Rudakov, A.P. (1970). Polyimides: a new class of thermally stable polymers. Prog. Mater. Sci. Ser. 7: 13–57.

Baetens, R., Jelle, B.P., and Gustavsen, A. (2011). Aerogel insulation for building applications: a state-of-the-art review. Energy Build. 43: 761–769, https://doi.org/10.1016/j.enbuild.2010.12.012.

Barbetta, A. and Cameron, N.R. (2004). Morphology and surface area of emulsion-derived (PolyHIPE) solid foams prepared with oil-phase soluble porogenic solvents: Span 80 as surfactant. Macromolecules 37: 3188–3201, https://doi.org/10.1021/ma0359436.

Bessonov, M.I., Koton, M.M., Kudryavtsev V.V., and Lauis, L.A. (1987). *Polyimides, thermally stable polymers*. Plenum, New York.

Bhumgara, Z. (1995). Polyhipe foam materials as filtration media. Filtr. Sep. 32: 245–251, https://doi.org/10.1016/S0015-1882(97)84048-7.

Braun, R.D. and Manning, R.M. (2007). Mars exploration entry, descent, and landing challenges. J. Spacecraft Rockets 44: 310–323, https://doi.org/10.2514/1.25116.

Brinker, C.J. and Scherer, G. (1990). *Sol-gel science: the physics and chemistry of sol-gel processing*. Academic Press, New York, pp. 96–233.

Cashman, J.L., Nguyen, B.N., Dosa, B., and Meador, M.A.B. (2020). Flexible polyimide aerogels derived from the use of a neopentyl spacer in the backbone, ACS Appl. Polym. Mater. 2: 2179–2189, https://doi.org/10.1021/acsapm.0c00153.

Daniel, C., Sannino, D., and Guerra, G. (2008). Syndiotactic polystyrene aerogels: adsorption in amorphous pores and absorption in crystalline nanocavities. Chem. Mater. 20: 577–582, https://doi.org/10.1021/cm702475a.

Duan, Y., Jana, S.C., Lama, B., and Espe, M. (2013). Reinforcement of silica aerogels using silane end-capped polyurethanes. Langmuir 29: 6156–6165, https://doi.org/10.1021/la4007394.

Duan, Y., Jana, S.C., Reinsel, A.M., Lama, B., and Espe, M.P. (2012). Surface modification and reinforcement of silica aerogels using polyhedral oligomeric silsesquioxanes. Langmuir 28: 15362–15371, https://doi.org/10.1021/la302945b.

Fesmire, J.E. and Sass, J.P. (2008). Aerogel insulation applications for liquid hydrogen launch vehicle tanks. Cryogenics 48: 223–231, https://doi.org/10.1016/j.cryogenics.2008.03.014.

Forest, L., Gibiat, V., and Hooley, A. (2001). Impedance matching and acoustic absorption in granular layers of silica aerogels. J. Non-Cryst. Solids 285: 230–235, https://doi.org/10.1016/s0022-3093(01)00458-6.

Grace, H.P. (1982). Dispersion phenomena in high viscosity fluid systems and application of static mixers as dispersion devices in such systems. Chem. Eng. Commun. 14: 225–277, https://doi.org/10.1080/00986448208911047.

Gu, S., Li, Z., Miyoshi, T., and Jana, S.C. (2015). Polybenzoxazine aerogels with controllable pore structures. RSC Adv. 5: 26801–26805, https://doi.org/10.1039/C5RA02635K.

Gu, S., Zhai, C., and Jana, S.C. (2016). Aerogel microparticles from oil-in-oil emulsion systems. Langmuir 32: 5637–5645, https://doi.org/10.1021/acs.langmuir.6b01043.

Guo, H., Meador, M.A.B., Cashman, J.L., Tresp, D., Dosa, B., Scheiman, D.A., and McCorkle, L.S. (2020). Flexible polyimide aerogels with dodecane links in the backbone structure. ACS Appl. Mater. Interfaces 12: 33288–33296, https://doi.org/10.1021/acsami.0c09321.

Guo, H., Meador, M.A.B., McCorkle, L., Quade, D.J., Guo, J., Hamilton, B., Cakmak, M., and Sprowl, G. (2011). Polyimide aerogels cross-linked through amine functionalized polyoligomeric silsesquioxane. ACS Appl. Mater. Interfaces 3: 546–552, https://doi.org/10.1021/am101123h.

Jones, S.M. (2006). Aerogel: space exploration applications. J. Sol. Gel Sci. Technol. 40: 351–357, https://doi.org/10.1007/s10971-006-7762-7.

Joo, P., Yao, Y., Teo, N., and Jana, S.C. (2021). Modular aerogel brick fabrication via 3D-printed molds. Addit. Manuf. 46: 102059, https://doi.org/10.1016/j.addma.2021.102059.

Kawagishi, K., Saito, H., Furukawa, H., and Horie, K. (2007). Superior nanoporous polyimides via supercritical CO_2 drying of jungle-gym-type polyimide gels. Macromol. Rapid Commun. 28: 96–100, https://doi.org/10.1002/marc.200600587.

Kim, S.J., Chase, G., and Jana, S.C. (2015). Polymer aerogels for efficient removal of airborne nanoparticles. Sep. Purif. Technol. 156: 803–808, https://doi.org/10.1016/j.seppur.2015.11.005.

Kim, S.J., Chase, G., and Jana, S.C. (2016). The role of mesopores in achieving high efficiency airborne nanoparticle filtration using aerogel monoliths. Sep. Purif. Technol. 166: 48–54, https://doi.org/10.1016/j.seppur.2016.04.017.

Kim, S.J., Raut, P., Jana, S.C., and Chase, G. (2017). Electrostatically active polymer hybrid aerogels for airborne nanoparticle filtration. ACS Appl. Mater. Interfaces 9: 6401–6410, https://doi.org/10.1021/acsami.6b14784.

Kistler, S.S. (1932). Coherent expanded aerogels. J. Phys. Chem. 36: 52–64, https://doi.org/10.1021/j150331a003.

Kistler, S.S. (1935). The relation between heat conductivity and structure in silica aerogel. J. Phys. Chem. 39: 79–87, https://doi.org/10.1021/j150361a006.

Kocon, L., Despetis, F., and Phalippou, J. (1998). Ultralow density silica aerogels by alcohol supercritical drying. J. Non-Cryst. Solids 225: 96–100, https://doi.org/10.1016/s0022-3093(98)00322-6.

Kulkarni, A. and Jana, S.C. (2021). Surfactant-free syndiotactic polystyrene aerogel foams via pickering emulsion. Polymer 212: 123125, https://doi.org/10.1016/j.polymer.2020.123125.

Lee, J.K., Gould, G.L., and Rhine, W. (2009). Polyurea based aerogel for a high performance thermal insulation material. J. Sol. Gel Sci. Technol. 49: 209–220, https://doi.org/10.1007/s10971-008-1861-6.

Leventis, N., Sotiriou-Leventis, C., Chandrasekaran, N., Mulik, S., Larimore, Z.J., Lu, H., Churu, G., and Mang, J.T. (2010). Multifunctional polyurea aerogels from isocyanates and water. A structure–property case study. Chem. Mater. 22: 6692–6710, https://doi.org/10.1021/cm102891d.

Lin, W.-H. and Jana, S.C. (2021). Analysis of porous structures of cellulose aerogel monoliths and microparticles. Microporous Mesoporous Mater. 310: 110625, https://doi.org/10.1016/j.micromeso.2020.110625.

Mahadik-Khanolkar, S., Donthula, S., Sotiriou-Leventis, C., and Leventis, N. (2014). Polybenzoxazine aerogels. 1. High-yield room-temperature acid-catalyzed synthesis of robust monoliths, oxidative aromatization, and conversion to microporous carbons. Chem. Mater. 26: 1303–1317, https://doi.org/10.1021/cm403483p.

Mawhinney, K. and Jana, S.C. (2019). Design of emulsion-templated mesoporous–macroporous polyurea gels and aerogels. ACS Appl. Polym. Mater. 1: 3115–3129, https://doi.org/10.1021/acsapm.9b00762.

Mccusker, L.B., Liebau, F., and Engelhardt, G. (2001). Nomenclature of structural and compositional characteristics of ordered microporous and mesoporous materials with inorganic hosts (IUPAC Recommendations 2001). Pure Appl. Chem. 73: 381–394, https://doi.org/10.1351/pac200173020381.

Meador, M.A.B. (2014). Polyimide aerogels with three-dimensional cross-linked structure, US9309369B1.

Meador, M.A.B., Agnello, M., McCorkle, L., Vivod, S.L., and Wilmoth, N. (2016). Moisture-resistant polyimide aerogels containing propylene oxide links in the backbone. ACS Appl. Mater. Interfaces 8: 29073–29079, https://doi.org/10.1021/acsami.6b10248.

Meador, M.A.B., Alemán, C.R., Hanson, K., Ramirez, N., Vivod, S.L., Wilmoth, N., and McCorkle, L. (2015). Polyimide aerogels with amide cross-links: a low cost alternative for mechanically strong polymer aerogels. ACS Appl. Mater. Interfaces 7: 1240–1249, https://doi.org/10.1021/am507268c.

Meador, M.A.B., Malow, E.J., Silva, R., Wright, S., Quade, D., Vivod, S.L., Guo, H., Guo, J., and Cakmak, M. (2012). Mechanically strong, flexible polyimide aerogels cross-linked with aromatic triamine. ACS Appl. Mater. Interfaces 4: 536–544, https://doi.org/10.1021/am2014635.

Meador, M.A.B., McMillon, E., Sandberg, A., Barrios, E., Wilmoth, N.G., Mueller, C.H., and Miranda, F.A. (2014). Dielectric and other properties of polyimide aerogels containing fluorinated blocks. ACS Appl. Mater. Interfaces 6: 6062–6068, https://doi.org/10.1021/am405106h.

Meador, M.A.B., Scherzer, C.M., Vivod, S.L., Quade, D., and Nguyen, B.N. (2010). Epoxy reinforced aerogels made using a streamlined process. ACS Appl. Mater. Interfaces 2: 2162–2168, https://doi.org/10.1021/am100422x.

Menner, A. and Bismarck, A. (2006). New evidence for the mechanism of the pore formation in polymerising high internal phase emulsions or why PolyHIPEs have an interconnected pore network structure. Macromol. Symp. 242: 19–24, https://doi.org/10.1002/masy.200651004.

Menner, A., Haibach, K., Powell, R., and Bismarck, A. (2006). Tough reinforced open porous polymer foams via concentrated emulsion templating. Polymer 47: 7628–7635, https://doi.org/10.1016/j.polymer.2006.09.022.

Molau, G.E. (1965). Heterogeneous polymer systems. II. Mechanism of stabilization of polymeric oil-in-oil emulsions. J. Polym. Sci. A Gen. Pap. 3: 4235–4242, https://doi.org/10.1002/pol.1965.100031219.

Mosanenzadeh, S.G., Saadatnia, Z., Karamikamkar, S., Park, C.B., and Naguib, H.E. (2020). Polyimide aerogels with novel bimodal micro and nano porous structure assembly for airborne nano filtering applications. RSC Adv. 10: 22909–22920, https://doi.org/10.1039/d0ra03907a.

Nekouei, M. and Vanapalli, S.A. (2017). Volume-of-fluid simulations in microfluidic T-junction devices: influence of viscosity ratio on droplet size. Phys. Fluids 29: 032007, https://doi.org/10.1063/1.4978801.

Pajonk, G. (1991). Aerogel catalysts. Appl. Catal. 72: 217–266, https://doi.org/10.1016/0166-9834(91)85054-y.

Pandit, N., Trygstad, T., Croy, S., Bohorquez, M., and Koch, C. (2000). Effect of salts on the micellization, clouding, and solubilization behavior of pluronic F127 solutions. J. Colloid Interface Sci. 222: 213–220, https://doi.org/10.1006/jcis.1999.6628.

Pantoja, M., Boynton, N., Cavicchi, K.A., Dosa, B., Cashman, J.L., and Meador, M.A.B. (2019). Increased flexibility in polyimide aerogels using aliphatic spacers in the polymer backbone. ACS Appl. Mater. Interfaces 11: 9425–9437, https://doi.org/10.1021/acsami.8b20420.

Randall, J.P., Meador, M.A.B., and Jana, S.C. (2011). Tailoring mechanical properties of aerogels for aerospace applications. ACS Appl. Mater. Interfaces 3: 613–626, https://doi.org/10.1021/am200007n.

Richardson, J.F. and Zaki, W.N. (1954). Sedimentation and fluidisation: part 1. Chem. Eng. 32: 35–53.

Shinko, A., Jana, S.C., and Meador, M.A. (2015). Crosslinked polyurea aerogels with controlled porosity. RSC Adv. 5: 105329–105338, https://doi.org/10.1039/c5ra20788f.

Silverstein, M.S. (2014). PolyHIPEs: recent advances in emulsion-templated porous polymers. Prog. Polym. Sci. 39: 199–234, https://doi.org/10.1016/j.progpolymsci.2013.07.003.

Smallwood, I.M. (2012). *Handbook of organic solvent properties*. Elsevier, New York, USA, pp. 1–306.

Tebboth, M., Menner, A., Kogelbauer, A., and Bismarck, A. (2014). Polymerised high internal phase emulsions for fluid separation applications. Curr. Opin. Chem. Eng. 4: 114–120, https://doi.org/10.1016/j.coche.2014.03.001.

Teo, N. and Jana, S.C. (2017). Open cell aerogel foams via emulsion templating. Langmuir 33: 12729–12738, https://doi.org/10.1021/acs.langmuir.7b03139.

Teo, N. and Jana, S.C. (2018). Solvent effects on tuning pore structures in polyimide aerogels. Langmuir 34: 8581–8590, https://doi.org/10.1021/acs.langmuir.8b01513.

Teo, N. and Jana, S.C. (2019). A surfactant-free process for fabrication of polyimide aerogel microparticles. Langmuir 35: 2303–2312, https://doi.org/10.1021/acs.langmuir.8b03841.

Teo, N., Gu, Z., and Jana, S.C. (2018). Polyimide-based aerogel foams via emulsion-templating. Polymer 157: 12729–12738, https://doi.org/10.1016/j.polymer.2018.10.030.

Teo, N., Jin, C., Kulkarni, A., and Jana, S.C. (2020). Continuous fabrication of core-shell aerogel microparticles using microfluidic flows. J. Colloid Interface Sci. 561: 772–781, https://doi.org/10.1016/j.jcis.2019.11.053.

Teo, N., Joo, P., Amis, E., and Jana, S.C. (2019). Development of intricate aerogel articles using fused filament fabrication. ACS Appl. Polym. Mater. 1: 1749–1756, https://doi.org/10.1021/acsapm.9b00301.

Wang, X. and Jana, S.C. (2013). Tailoring of morphology and surface properties of syndiotactic polystyrene aerogels. Langmuir 29: 5589–5598, https://doi.org/10.1021/la400492m.

Wong, L.L.C., Villafranca, P.M.B., Menner, A., and Bismarck, A. (2013). Hierarchical polymerized high internal phase emulsions synthesized from surfactant-stabilized emulsion templates. Langmuir 29: 5952–5961, https://doi.org/10.1021/la3047643.

Yoldas, B.E., Annen, M.J., and Bostaph, J. (2000). Chemical engineering of aerogel morphology formed under nonsupercritical conditions for thermal insulation. Chem. Mater. 12: 2475–2484, https://doi.org/10.1021/cm9903428.

Zapryanov, Z., Malhotra, A.K., Aderangi, N., and Wasan, D.T. (1983). Emulsion stability: an analysis of the effects of bulk and interfacial properties on film mobility and drainage rate. Int. J. Multiphas. Flow 9: 105–129, https://doi.org/10.1016/0301-9322(83)90047-2.

Zebida, O.A. (2011). *Aerogel filters for removal of nanometric airborne particles*. LAMBERT Academic Publishing (LAP), Chisinau, Republic of Moldova.

Zhai, C. and Jana, S.C. (2017). Tuning porous networks in polyimide aerogels for airborne nanoparticle filtration. ACS Appl. Mater. Interfaces 9: 30074–30082, https://doi.org/10.1021/acsami.7b09345.

Zhou, B., Shen, J., Yuehua, W., Wu, G., and Ni, X. (2007). Hydrophobic silica aerogels derived from polyethoxydisiloxane and perfluoroalkylsilane. Mater. Sci. Eng. 27: 1291–1294, https://doi.org/10.1016/j.msec.2006.06.032.

Supplementary Material: The online version of this article offers supplementary material (https://doi.org/10.1515/ipp-2022-4248).